

Sideband Modulation by Sub-Cycle Interference

S. Eckart,^{1*} D. Trabert,¹ K. Fehre,¹ A. Geyer,¹ J. Rist,¹
K. Lin,¹ F. Trinter,^{1,2} L. Ph. H. Schmidt,¹ M. S. Schöffler,¹
T. Jahnke,¹ M. Kunitski,¹ R. Dörner¹

¹ Institut für Kernphysik, Goethe-Universität, Max-von-Laue-Str. 1, 60438 Frankfurt, Germany.

² Molecular Physics, Fritz-Haber-Institut der Max-Planck-Gesellschaft,
Faradayweg 4-6, 14195 Berlin, Germany.

*E-mail: eckart@atom.uni-frankfurt.de

We experimentally and theoretically show that the electron energy spectra strongly depend on the relative helicity in highly intense, circularly polarized two-color laser fields which is an unexpected finding. The employed counter-rotating two-color (CRTC) fields and the co-rotating two-color (CoRTC) fields are both a superposition of circularly polarized laser pulses at a central wavelength of 390 nm and 780 nm (intensitiy ratio $I_{390}/I_{780} \approx 250$). For the CRTC field, the measured electron energy spectrum is dominated by peaks that are spaced by 3.18 eV (corresponds to the photon energy of light at a wavelength of 390 nm). For the CoRTC field, we observe additional energy peaks (sidebands). Using our semi-classical, trajectory-based models, we conclude that the sideband intensity is modulated by a sub-cycle interference, which sensitively depends on the relative helicity in circularly polarized two-color fields.

Introduction

When a single atom or molecule is irradiated with a highly intense light field, it can be ionized by non-resonant absorption of more photons than necessary to overcome the binding energy (1). This phenomenon of above threshold ionization (ATI) (2–6) leads to peaks in the electron energy spectrum that are spaced by the photon energy. When photons at a second wavelength are added to the light field, the question arises what determines the relative amount of photons that is absorbed from each of the two single colors. A trivial control parameter is the intensity ratio of the two single colors. Here we show that the relative helicity of the two single colors can be an additional, very effective control parameter.

For light at a central wavelength of 390 nm, the ATI comb in the electron energy spectrum has a spacing of $E_{390}^{ph} = 3.18 \text{ eV}$. If the light field comprises photons of a second energy $E_{780}^{ph} = 1.59 \text{ eV}$ in addition, the electrons can have discrete energies of:

$$E_{\text{elec}} = N_{390} \cdot E_{390}^{ph} + N_{780} \cdot E_{780}^{ph} - U_p^{\text{eff}} - I_p \quad (1)$$

Here, N_{390} is the number of absorbed photons with an energy of E_{390}^{ph} and N_{780} denotes the corresponding number of photons at an energy of $E_{780}^{ph} = 0.5 \cdot E_{390}^{ph}$. Equation 1 indicates that in addition to the ionization potential I_p also the ponderomotive potential U_p^{eff} of the two-color laser field has to be taken into account (4, 7). To demonstrate the helicity dependence, we choose a two-color field that is the superposition of an intense circularly polarized light field at a central wavelength of 390 nm ($I_{390} = 1.2 \cdot 10^{14} \text{ W/cm}^2$, peak electric field of 0.041 a.u.) and a much weaker circularly polarized light field at a central wavelength of 780 nm ($I_{780} = 4.7 \cdot 10^{11} \text{ W/cm}^2$, peak electric field of 0.0026 a.u.). According to energy conservation (Eq. 1), all possible final electron energies are spaced by E_{780}^{ph} (independent of the helicities of the two single colors). Final electron energies, E_{elec} , that can be reached for even (odd) values of N_{780} are called ATI (sideband) peaks. This is equivalent to referring to the peaks in the electron

energy spectrum which result from the photons of the dominating color (at a central wavelength of 390 nm) as ATI peaks and those in between as sidebands.

Originally, counter-rotating two-color (CRTC) fields were introduced aiming at the production of circularly polarized high-harmonics (8, 9). In the past years, CRTC fields and co-rotating two-color (CoRTC) fields (10) have been used to, e.g., retrieve properties of the electronic wave function (11), obtain attosecond time information (7, 12), investigate non-adiabatic offsets in momentum space at the tunnel exit (13), observe sub-cycle interference (14–16), and to control non-sequential double ionization (17–19). Moreover, it has been shown that the ionization pathways in multi-photon ionization are different comparing counter-rotating two-color and orthogonally polarized two-color fields (20) and it was discovered that the absolute ionization probability (independent of the electron energy) can be different for CRTC fields and CoRTC fields (21).

Results

Figure 1 shows the measured electron energy spectra upon the single ionization of argon comparing the counter-rotating two-color field (CRTC, opposite helicity of the two colors) and the co-rotating two-color field (CoRTC, same helicity of the two colors). It is evident that the CRTC field produces ATI peaks which are spaced by E_{390}^{ph} and that the sidebands are hardly visible. For the CoRTC field, the sidebands are as intense as the ATI peaks resulting in an energy spectrum that is a comb with a spacing of E_{780}^{ph} . From the measured energy spectra it appears that there should be a straightforward explanation using selection rules or propensity rules. However, we were not able to find any explanation for our experimental results using established concepts in the strong field regime (22–24).

In this paper, we will explain the pronounced difference in sideband intensity, that is seen in Fig. 1, using a time-dependent perspective of wave packet creation by tunnel ionization. For

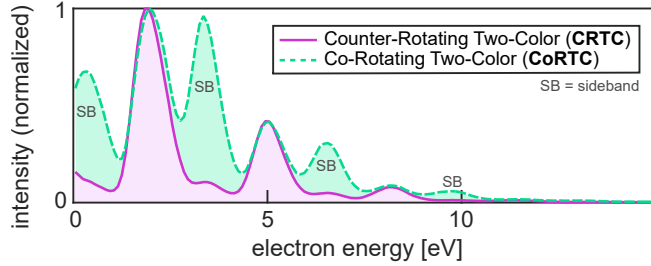


Figure 1: Measured electron energy spectra depend on the relative helicity of circularly polarized two-color fields. The measured electron energy spectra upon single ionization of argon are shown for a CRTC and a CoRTC field. The sidebands are very intense for the CoRTC field and are hardly visible for the CRTC field. Sideband peaks are labeled with “SB”.

a circularly polarized single-color laser field one can understand the origin of ATI peaks as a consequence of energy conservation or as a result of the periodic structure of the electron release times which acts as a grating in the time-domain and gives rise to an inter-cycle interference that leads to the periodic ATI structure in electron energy (25). For CRTC and CoRTC fields, there is an additional sub-cycle interference which can lead to an additional modulation of the possible energy peaks according to Eq. 1. In this paper, we show that this sub-cycle interference is very different for CRTC and CoRTC fields and that this will elegantly explain our experimental findings.

Figures 2A and 2B depict the combined laser electric fields and the negative vector potentials that are used in the experiment. The Lissajous curves of the CRTC field and the CoRTC field are very similar. The weak laser pulse at a central wavelength of 780 nm only induces a small distortion and gives rise to a three-fold (one-fold) symmetry in the CRTC (CoRTC) field. Figure 2C shows the measured electron momentum distribution in the plane of polarization for the CRTC field (see Methods). This electron momentum distribution shows almost no three-fold symmetric features and is dominated by the ATI peaks. Upon inversion of the helicity of the laser pulse at a central wavelength of 780 nm, the measured electron momentum distribution changes drastically, as can be seen in Fig. 2D. A strong one-fold symmetric pattern of

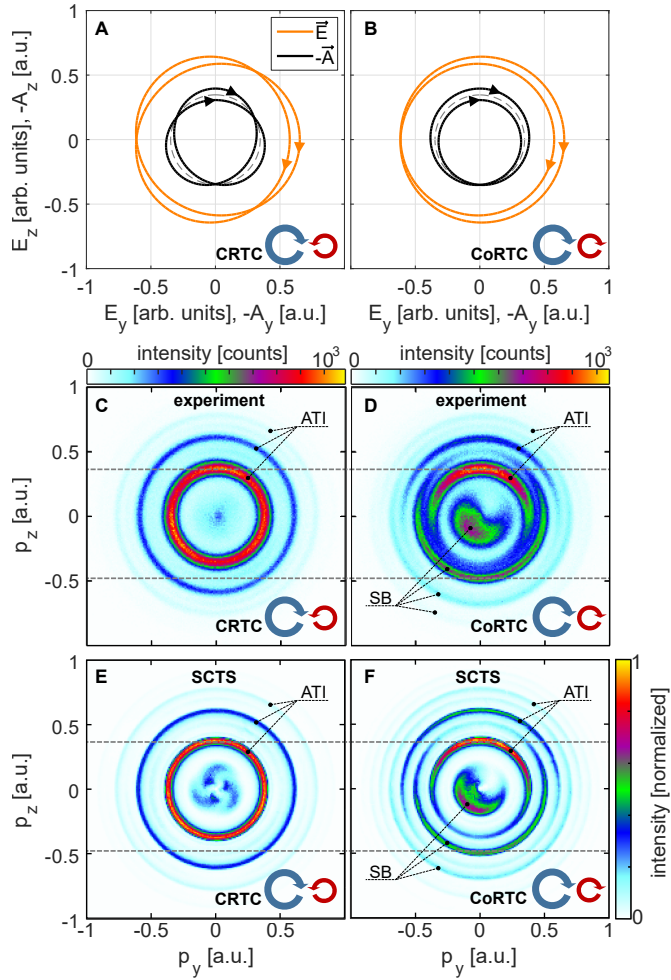


Figure 2: Experimental and theoretical electron momentum distributions for counter- and co-rotating two-color fields. (A) The combined electric field \vec{E} and the negative vector potential $-\vec{A}$ for the counter-rotating two-color (CRTC) field. (B) The corresponding co-rotating two-color (CoRTC) field. The helicities of the two colors and the temporal evolution of \vec{E} and $-\vec{A}$ are indicated with arrows. (C) [(D)] The measured electron momentum distribution in the plane of polarization for the laser field shown in A [B]. The electron energy spectrum shown in Fig. 1 is based on the same data as C and D. (E) [(F)] Electron momentum distribution in the plane of polarization for the CRTC [CoRTC] field that is obtained using the semi-classical two-step model (SCTS). Horizontal dashed gray lines guide the eye. Sideband peaks are labeled with “SB”.

alternating half-rings is observed. In particular, certain regions that are empty in Fig. 2C are populated in Fig. 2D, giving rise to the sidebands in the electron energy spectrum (see Fig. 1). Fig. 2E and 2F show the results from our full theoretical model that is a semi-classical two-step (SCTS) model (26) with tunneling probabilities from saddle-point strong field approximation (see Methods). Besides the typical overestimation of the intensity at low electron energies (16), the results from this SCTS model show excellent agreement with the experimental findings.

A Simplified Model (HASE model)

The alternating half-ring pattern for CoRTC fields by itself is a well-documented phenomenon (7, 11, 12). The fact that the existence of sidebands depends on the relative helicity of the two single colors has not yet been described to the best of our knowledge. What is the microscopic origin of this huge difference in the energy spectra comparing CoRTC and CRTC fields? In the following, we show that the intensity of the ATI peaks and the sidebands are modulated by a sub-cycle interference. For CoRTC fields, this sub-cycle interference has recently been termed holographic angular streaking of electrons (HASE) and modeled using a trajectory-based, semi-classical model (HASE model) (12). In comparison to the full SCTS model, the HASE model neglects Coulomb interaction after tunneling, sets the momentum in the light-propagation direction to zero, uses only a two-cycle laser pulse without envelope and assumes that the tunneling probability is independent of the initial conditions. (The tunneling probability is time-independent and does not depend on the initial momentum at all.) Thus, the HASE model can be viewed to be a simplified version of the SCTS model and can be summarized as follows: We assume that the electrons are released with an initial momentum \vec{p}_0 that fulfills the condition

$$\vec{p}_0 \cdot \vec{E}(t_0) = 0 \quad (2)$$

which indicates that \vec{p}_0 is perpendicular to the tunneling direction. Here $\vec{E}(t_0)$ is the laser electric field at the time the electron tunnels, t_0 . Moreover, \vec{p}_0 is zero along the light propagation direction since the HASE model is a two-dimensional simulation. The final electron momentum \vec{p}_f is the vectorial sum of the initial momentum upon tunneling and the negative vector potential at the electron's release time $-\vec{A}(t_0)$:

$$\vec{p}_f = -\vec{A}(t_0) + \vec{p}_0 \quad (3)$$

Since for every angle in the plane of polarization there are two different vector potentials, there are exactly two possible initial release times (t_1 and t_2) within one cycle of the two-color laser field that lead to the same final electron momentum \vec{p}_f . One cycle of the two-color laser field has a periodicity of T_{780} (duration of one optical cycle of light at a wavelength of 780 nm). For each final electron momentum in the plane of polarization ($p_y p_z$ -plane), an optimization algorithm searches for the initial release times t_1 and t_2 . Having found the two initial release times t_1 and t_2 within one cycle of the two-color laser field, one can consider a second, subsequent, cycle of the two-color laser field. This allows for the modeling of sub- and inter-cycle interference on the same footing (12). Therefore, the release times $t_3 = t_1 + T_{780}$ and $t_4 = t_2 + T_{780}$ are the equivalent release times in the second light cycle that lead to the same final momentum \vec{p}_f . Thus, within two cycles of the laser field, exactly four release times t_n can be identified for each final momentum \vec{p}_f (with the trajectory number $n \in \{1, 2, 3, 4\}$). Knowing these release times and neglecting Coulomb interaction after tunneling, the semi-classical phase for these trajectories is given by (12):

$$\phi_n(\vec{p}_f, t_f) = \frac{1}{\hbar} \left(I_p t_n - \int_{t_n}^{t_f} \frac{p_y^2(t) + p_z^2(t)}{2m_e} dt \right) \quad (4)$$

Here, $m_e = 1$ a.u. is the electron's mass, $\hbar = 1$ a.u. is the reduced Planck constant, and $I_p = 15.76$ eV is the ionization potential of argon. In Eq. 4, the first summand models the phase evolution of the electron in its bound state and the second term models the phase evolution after

tunneling by the integral of the electron's kinetic energy with respect to time. Note that the choice of t_f only affects the absolute phase of all four trajectories but not the relative phase of the trajectories. We always choose $t_f = t_4$ as in Ref. (12). Assuming that all four trajectories have the same probability to exist (see Ref. (12) for details), the semi-classically modeled wave function at a given final electron momentum \vec{p}_f is:

$$\Psi(\vec{p}_f) = \sum_{n=1}^4 \exp(i\phi_n(\vec{p}_f, t_f)) \quad (5)$$

Within the HASE model, $P_{\text{complete}}(\vec{p}_f) = |\Psi(\vec{p}_f)|^2$ describes intensity modulations in momentum space that are due to sub-cycle and inter-cycle interference. Trajectories are only calculated for final electron momenta \vec{p}_f with an absolute value between 0.2 a.u. and 1 a.u. In short, the HASE model is a very intuitive and transparent model that is defined by Eq. 2 - Eq. 5.

Results of the HASE model

The results from the HASE model are shown in Fig. 3. Figures 3A and 3B show the absolute value of the negative vector potential $|\vec{A}(t)|$ for two optical cycles of the CRTC and the CoRTC field, respectively. The possible ranges of the release times t_1, t_2, t_3 , and t_4 are colored in blue, green, yellow, and red and are labeled with the corresponding trajectory number n . It should be noted that for every point in final momentum space, the values of t_n can differ but the allowed ranges, that are indicated with colors, do not change as a function of \vec{p}_f (12, 27). Figure 3C [3D] shows the semi-classically modeled intensity $P_{\text{complete}}(\vec{p}_f) = |\Psi(\vec{p}_f)|^2$ in final electron momentum space for the CRTC [CoRTC] field. Strikingly, the semi-classical result for the CRTC field shows almost no intensity at the energies that correspond to the sidebands (Fig. 3C). The alternating half-ring structure is only observed for the CoRTC field (Fig. 3D). For the CRTC field, only a weak modulation in intensity as a function of the angle in the plane of polarization is visible. This is all in excellent agreement with the findings presented in Fig.

2. The fact that the HASE model succeeds to model the experimentally observed interference pattern shows that the HASE model captures the essential physics of the studied scenarios.

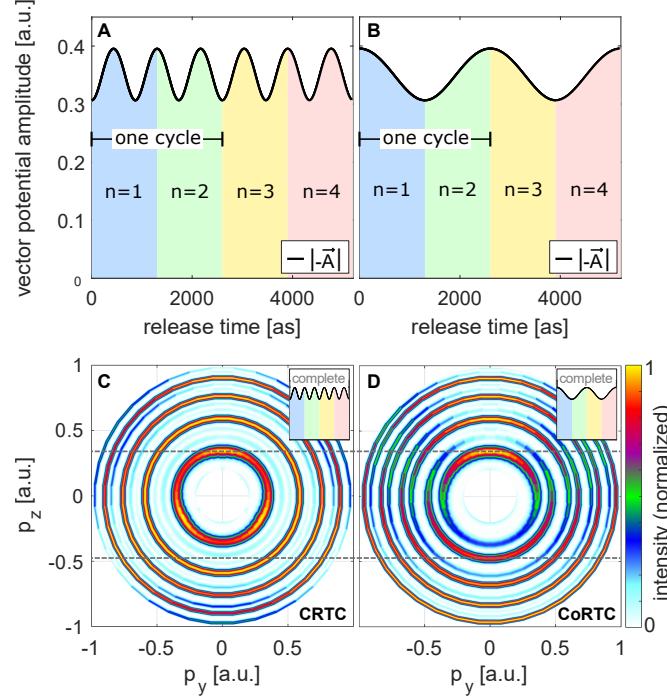


Figure 3: The simplified theoretical model (HASE model) reproduces the interference patterns for counter- and co-rotating two-color fields. (A) [(B)] The absolute value of the negative vector potential $| - |vec{A}(t)|$ for two optical cycles of the CRTC [CoRTC] field. The four colored regions indicate the temporal windows of the corresponding electron release times t_n and the corresponding trajectory number n . The duration of one cycle of the combined electric field is indicated. (C) [(D)] The semi-classically modeled intensity in final electron momentum space $P_{\text{complete}}(\vec{p}_f) = \left| \sum_{n=1}^4 \exp(i\phi_n(\vec{p}_f)) \right|^2$ for the CRTC [CoRTC] field (see text related to Eq. 5). Horizontal dashed gray lines guide the eye in C and D.

Discussion

What is the reason for the obvious difference comparing the CRTC and the CoRTC field? Since our semi-classical results only model sub-cycle and inter-cycle interference, we inspect the relative phases of the interfering semi-classical trajectories. To this end, the intensity

$P_{\text{sub}} = |\exp(i\phi_1) + \exp(i\phi_2)|^2$ is visualized for the CRTC field as a function of the final electron momentum in the plane of polarization (Fig. 4A). High intensities indicate constructive interference and therefore a phase difference $\phi_2 - \phi_1$ that is close to multiples of 2π . This interference pattern is due to a sub-cycle interference since the difference in the release time of the two contributing trajectories is $t_2 - t_1$, which is shorter than one light cycle (see Fig. 3). Figure 4B shows the same for the CoRTC field. Comparison of Figs. 4A and 4B reveals that the phase difference $\phi_2 - \phi_1$ depends more strongly on the angle in the plane of polarization for the CoRTC field. This is underlined by comparing the interference pattern near the gray dashed circles that guide the eye in Figs. 4A and 4B. In a next step, the relative phase $\phi_3 - \phi_1$ is investigated. Figures 4C and 4D visualize $P_{\text{inter}} = |\exp(i\phi_1) + \exp(i\phi_3)|^2$. Because the time difference $t_3 - t_1$ is exactly as long as one light cycle, the interference is an inter-cycle interference. Figures 4C and 4D show the same distribution which is independent of the angle in the plane of polarization. The two inner rings with high intensity in Figs. 4C and 4D are highlighted with gray dashed circles. If high intensity is observed for P_{sub} , then $\phi_2 - \phi_1$ is close to multiples of 2π . And if high intensity is observed for P_{inter} , then $\phi_3 - \phi_1$ is close to multiples of 2π . Thus, if high intensity is observed for P_{sub} and P_{inter} , then $\phi_3 - \phi_2$ is also close to multiples of 2π . Further, the relative phase $\phi_4 - \phi_3$ is the same as $\phi_2 - \phi_1$ because of the periodicity of the light field (see Fig. 3). This allows to conclude, that a high intensity for $P_{\text{sub}}(\vec{p}_f)$ and $P_{\text{inter}}(\vec{p}_f)$ implies that all four trajectories are interfering constructively for this \vec{p}_f which leads to high intensity in final electron momentum space ($P_{\text{complete}}(\vec{p}_f)$). Comparison of Fig. 3D with Fig. 4B and Fig. 4D reveals that it is in fact the interplay of sub- and inter-cycle interference that determines the final electron momentum distribution P_{complete} and gives rise to the alternating half-ring pattern for the CoRTC field. The weak modulations for the CRTC field that are seen in Fig. 3C can be explained in full analogy.

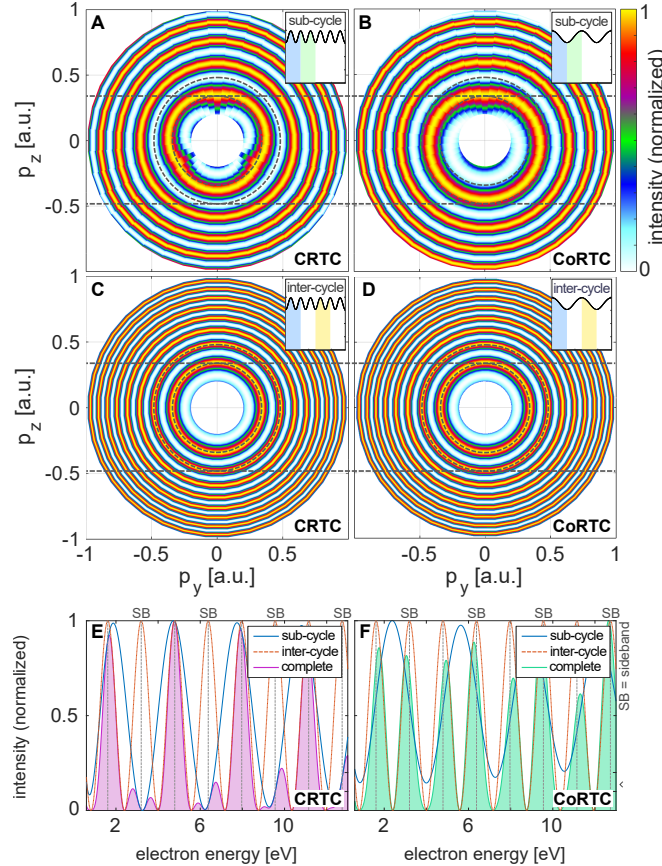


Figure 4: Sub-cycle interference modulates sideband intensity. (A) [(B)] Intensity modulation due to sub-cycle interference $P_{\text{sub}} = |\exp(i\phi_1) + \exp(i\phi_2)|^2$ for the CRTC [CoRTC] field. The possible release times of the trajectories for ϕ_1 and ϕ_2 are labeled with $n = 1$ and $n = 2$ in Fig. 3. (C), (D) Intensity modulation due to inter-cycle interference $P_{\text{inter}} = |\exp(i\phi_1) + \exp(i\phi_3)|^2$ (release times are labeled with $n = 1$ and $n = 3$ in Fig. 3). (E) Interference patterns from A, C, and Fig. 3C as a function of the electron energy for the CRTC field. (F) The same as E for the CoRTC field. Vertical gray dashed lines indicate the peaks of the inter-cycle interference. The dashed gray lines in A-D are the same in all four panels and guide the eye.

These insights allow for a microscopic explanation of the experimental findings presented in Fig. 1 and Fig. 2: The inter-cycle interference P_{inter} , that is seen in Figs. 4C and 4D, reflects a comb of allowed final electron energies that is independent of the angle in the polarization plane. This is in line with the allowed electron energies according to energy conservation (see Eq. 1). The finding that the sideband intensity depends on the relative helicity of the two colors is explained by a sub-cycle interference that depends on the angle in the polarization plane and is very different for the CRTC and the CoRTC field. Figures 4E and 4F illustrate this in energy space showing the energy spectra of the momentum distributions P_{sub} , P_{inter} , and P_{complete} . It is evident that the sub-cycle interference is very different comparing the CRTC and the CoRTC field: For the CRTC field, the sub-cycle interference is destructive at the energies that belong to the sidebands which leads to a strong suppression of sideband intensity in the corresponding final spectra. For the CoRTC field the sub-cycle interference attenuates ATI peaks and sidebands similarly but at different angle in the plane of polarization in final momentum space. In particular, it is evident from Fig. 4B that it is not possible to find an electron energy for which the sub-cycle interference is destructive for all angles in the polarization plane which explains why the curve for the sub-cycle interference pattern as a function of energy (see Fig. 4F) is bigger than zero for all electron energies.

Conclusion

In conclusion, our experimental results show an unexpected dependence of sideband intensity on the relative helicity in circularly polarized two-color light fields. We have used two different trajectory-based, semi-classical models that both reproduce the almost complete suppression of sideband intensity for the CRTC field. The modulation of the sideband intensity is a consequence of the differences in sub-cycle interference comparing CRTC and CoRTC fields. Our findings enable a better understanding of above-threshold ionization and are an important in-

sight regarding the coherent control of electrons. The overall ionization probability is governed by the 2ω field which is about 100 times more intense than the ω field. The emission of an entire class of electrons (sideband electrons) can be switched on and off on femtosecond timescales by employing an ω field with time-dependent polarization (28). This is similar to a transistor in electronics and would represent an electron emitter that is powered by a strong laser field at 2ω (“transistor’s collector”) and can be controlled by the helicity (which is equivalent to a relative phase for a light wave or to angular momentum for a photon) of a relatively weak laser pulse at a different frequency ω (“transistor’s base”).

Materials and Methods

Experimental Setup

The two-color fields are generated using a 200 μm BBO to frequency double 780 nm laser pulses (KMLabs Dragon, 40 fs FWHM, 8 kHz) using the same optical setup as in Refs. (13, 18, 29). We estimate the uncertainty of the absolute intensity for 780 nm and 390 nm to be 50% and 20%, respectively. The three-dimensional electron momentum distributions from single ionization of argon presented in this work have been measured using cold-target recoil-ion momentum spectroscopy (COLTRIMS) (30, 31). The length of the electron and ion arm was 378 mm and 67.8 mm, respectively. Homogeneous electric and magnetic fields of 11.4 V cm^{-1} and 8.6 G, respectively, guided electrons and ions towards time- and position-sensitive microchannel plate detectors with hexagonal delay-line anodes (31). During the measurement, we switch the helicity of the laser pulse at 780 nm every 240 seconds to minimize systematic errors. The total ionization rate does not depend significantly on the relative helicity.

SCTS Calculation

The semi-classical two-step (SCTS) simulation is based on the procedure described in Ref.

(26). Instead of using Eq. 9 from Ref. (26) we use the ionization probability from saddle-point strong field approximation (SFA) (6, 32, 33). In SFA the ionization probability for a circularly polarized light field depends on the frequency of the light field ω_{SFA} , the magnitude of the instantaneous electric field E_{SFA} , the ionization potential I_p , the momentum in the light propagation direction p_{x0} at the tunnel exit and the initial momentum at the tunnel exit which is in the plane of polarization and perpendicular to the tunnel exit p_0 . For our SCTS simulations we use $\omega_{\text{SFA}} = 2\omega$ with $\omega = 0.0584$ a.u. and hereby neglect the changes in ionization probability that are due to the sub-cycle of changes in angular frequency. This is a good approximation because the condition $I_{780} \ll I_{390}$ is fulfilled in our experiment. Neglecting the pre-exponential factor in saddle-point SFA, the instantaneous ionization probability can be approximated by (33, 34):

$$P = \exp \left(-\frac{2 \cdot I_p^{\text{eff}}}{\omega_{\text{SFA}} \cdot \gamma_{\text{eff}}^2} \left[2 \cdot q \cdot C \cdot \text{acosh}(C) - 2 \cdot q \cdot \sqrt{(C^2 - 1)} \right] \right) \quad (6)$$

Here, the following definitions are used:

$$A_{\text{SFA}} = E_{\text{SFA}} / \omega_{\text{SFA}} \quad (7)$$

$$q = (A_{\text{SFA}} + p_0) / A_{\text{SFA}} \quad (8)$$

$$I_p^{\text{eff}} = I_p + 0.5 \cdot p_{x0}^2 \quad (9)$$

$$\gamma_{\text{eff}} = \sqrt{(2 \cdot I_p^{\text{eff}})} / A_{\text{SFA}} \quad (10)$$

$$C = (1 + q^2 + \gamma_{\text{eff}}^2) / (2 \cdot q) \quad (11)$$

Therefore, the tunneling probability P in our SCTS model incorporates non-adiabaticity (6, 13) and is a function of E_{SFA} , p_{x0} and p_0 . The tunnel exit for each trajectory is obtained by solving Eq. (5) from Ref. (35) and afterwards each semi-classical trajectory is propagated in the $1/r$ -potential in the presence of the time-dependent laser electric field. We use a laser field with a total duration of 12 cycles that has a sine-square envelope and calculate 250 million semi-classical trajectories for the CoRTC and the CRTC scenario. Convergence of the simulations is

tested by varying the bin size of the grid and the method of “phase compression” is used (12, 36). The laser electric field in the SCTS model has been scaled down by 8% to improve agreement of experiment and theory for low energy electrons.

References

1. L. V. Keldysh, *Sov. Phys. JETP* **20**, 1307 (1965).
2. G. S. Voronov, N. B. Delone, *Sov. Phys. JETP* **23**, 54 (1966).
3. P. Agostini, F. Fabre, G. Mainfray, G. Petite, N. K. Rahman, *Phys. Rev. Lett.* **42**, 1127 (1979).
4. R. R. Freeman, *et al.*, *Phys. Rev. Lett.* **59**, 1092 (1987).
5. G. Petite, P. Agostini, H. Muller, *J. Phys. B* **21**, 4097 (1988).
6. M. Yu. Ivanov, M. Spanner, O. Smirnova, *J. Mod. Opt.* **52**, 165 (2005).
7. P. Ge, M. Han, Y. Deng, Q. Gong, Y. Liu, *Phys. Rev. Lett.* **122**, 013201 (2019).
8. W. Becker, B. N. Chichkov, B. Wellegehausen, *Phys. Rev. A* **60**, 1721 (1999).
9. A. Fleischer, O. Kfir, T. Diskin, P. Sidorenko, O. Cohen, *Nat. Photonics* **8**, 543 (2014).
10. C. A. Mancuso, *et al.*, *Phys. Rev. A* **91**, 031402(R) (2015).
11. M. Han, P. Ge, Y. Shao, Q. Gong, Y. Liu, *Phys. Rev. Lett.* **120**, 073202 (2018).
12. S. Eckart, *arXiv preprint, arXiv:2003.07249 (accepted at Phys. Rev. Research)* (2020).
13. S. Eckart, *et al.*, *Phys. Rev. Lett.* **121**, 163202 (2018).
14. L. Zhang, *et al.*, *Phys. Rev. A* **90**, 061401(R) (2014).

15. M. Richter, *et al.*, *Phys. Rev. Lett.* **114**, 143001 (2015).
16. S. Eckart, *et al.*, *Phys. Rev. A* **97**, 041402(R) (2018).
17. C. A. Mancuso, *et al.*, *Phys. Rev. Lett.* **117**, 133201 (2016).
18. S. Eckart, *et al.*, *Phys. Rev. Lett.* **117**, 133202 (2016).
19. K. Lin, *et al.*, *Phys. Rev. Lett.* **119**, 203202 (2017).
20. S. Kerbstadt, *et al.*, *New J. Phys.* **19**, 103017 (2017).
21. C. A. Mancuso, *et al.*, *Phys. Rev. A* **96**, 023402 (2017).
22. I. Barth, O. Smirnova, *Phys. Rev. A* **84**, 063415 (2011).
23. I. Barth, O. Smirnova, *Phys. Rev. A* **87**, 013433 (2013).
24. U. Fano, *Phys. Rev. A* **32**, 617 (1985).
25. D. G. Arbó, K. L. Ishikawa, K. Schiessl, E. Persson, J. Burgdörfer, *Phys. Rev. A* **81**, 021403(R) (2010).
26. N. I. Shvetsov-Shilovski, *et al.*, *Phys. Rev. A* **94**, 013415 (2016).
27. P. Eckle, *et al.*, *Science* **322**, 1525 (2008).
28. P. B. Corkum, N. H. Burnett, M. Y. Ivanov, *Opt. Lett.* **19**, 1870 (1994).
29. S. Eckart, *et al.*, *Nat. Phys.* **14**, 701 (2018).
30. J. Ullrich, *et al.*, *Rep. Prog. Phys.* **66**, 1463 (2003).
31. O. Jagutzki, *et al.*, *IEEE Trans. Nucl. Sci.* **49**, 2477 (2002).

32. D. Milošević, G. Paulus, D. Bauer, W. Becker, *J. Phys. B* **39**, R203 (2006).
33. S. V. Popruzhenko, *J. Phys. B* **47**, 204001 (2014).
34. D. Bauer, *Talk at the annual QUTIF meeting in Dornburg (Germany)* (2016).
35. N. I. Shvetsov-Shilovski, D. Dimitrovski, L. B. Madsen, *Phys. Rev. A* **85**, 023428 (2012).
36. S. G. Eckart, *Dissertation, Johann Wolfgang Goethe-Universität Frankfurt am Main* (2019).

Acknowledgments.

This work was funded by the German Research Foundation (DFG) through priority program SPP 1840 QUTIF.